Mechanical Systems and Signal Processing 260 (2026) 114929

Contents lists available at ScienceDirect

Mechanical Systems and Signal Processing

journal homepage: www.elsevier.com/locate/ymssp

Full Length Article

Modelling and characterization of the unzipping dynamics of dielectric fluid actuators☆

Marco Riva [a],*, Rajat Chaudhary [a], Sandra Dirè [a], Luca Fambri [a], Marco Fontana [b], Giacomo Moretti [a],*

[a] Department of Industrial Engineering, University of Trento, Trento, Italy
[b] Institute of Mechanical Intelligence, Scuola Sant'Anna, Pisa, Italy

ARTICLE INFO

Communicated by M.K. Role

Keywords:
Electrostatic actuation
Electroactive polymer
Actuator dynamics
Dielectric Fluid Actuator
Peano-HASEL
Charge retention

ABSTRACT

Dielectric Fluid Actuators (DFAs) are variable capacitors that contract as a result of electrostatic forces acting on a compliant multilayer structure composed of a polymer film and an insulating liquid. Differences in the dielectric time constants of the liquid and polymeric layers lead to charge retention at their interface, causing a decay in Maxwell stress that ultimately leads to a relaxation of the actuator stroke in the presence of a constant applied voltage. In this work, we introduce a new physics-based continuum framework that extends electrostatic force modelling from fixed parallel-plate capacitors to actuator-level modelling, by coupling continuum electrical dynamics with a lumped mechanical model of the DFA. The DFA is represented as a continuum of infinitesimal variable capacitors, each modelled using simple RC elements. The framework is experimentally validated on a simple multi-layer open-pouch DFA, and on an established layout of hydraulically amplified self-healing electrostatic actuator. Even with a simplified description of the material electrical response (e.g., constant resistivities) and lumped deformation mechanics, the framework captures the relevant trends in unzipping dynamics with respect to geometry and operating conditions (applied voltage and external forces). The proposed framework lays the foundations for electro-mechanical dynamic continuum modelling of DFAs.

1. Introduction

Dielectric fluid actuators (DFAs) are flexible transducers that leverage a variable-capacitance mechanism to contract upon the application of an electric field on a multilayer architecture composed of dielectric films and dielectric liquids [1–3]. In the last few years, DFAs have marked a major breakthrough in soft robotic actuation [4] thanks to their large actuation strains, high power density, and reliance on established high-voltage industry materials that enable scalable manufacturing [5].

Over the past few years, several DFA realizations have been proposed, differing in geometry and mechanical operating principles, yet consistently relying on a zipping kinematics to achieve contraction. A well-known class of DFAs, referred to as hydraulically amplified self-healing electrostatic (HASEL) actuators, exploit electrostatically induced pressurization of a dielectric liquid to produce work against a mechanical load [1,6,7]. Other architectures, such as electro-ribbon actuators [2,8] and electrostatic bellow

☆ Funded by the European Union (EU) under ERC Starting Grant project flEAP (GA: 101163668), and the Italian Ministry for University and Research (MUR) through the "Departments of Excellence 2023-27" program (L.232/2016) awarded to the Department of Industrial Engineering, University of Trento. Views and opinions expressed are however those of the authors only and do not necessarily reflect those of the EU, the ERC or the MUR. Neither the EU, the MUR nor the granting authorities can be held responsible for them.

* Corresponding authors.
E-mail addresses: marco.riva@unitn.it (M. Riva), giacomo.moretti@unitn.it (G. Moretti).

https://doi.org/10.1016/j.ymssp.2026.114929
Received 6 March 2026; Received in revised form 24 July 2026; Accepted 30 August 2026
Available online 12 September 2026

muscles [3,9], employ dielectric liquids at atmospheric pressure to generate large electric fields across variable dielectric gaps, while relying on the structural properties of the dielectric layers for force transmission.

These architectures have been demonstrated in a variety of mechatronic proof-of-concept applications, including tactile devices [7,10], tunable lenses [11], soft pumps [12,13], and autonomous robots [14,15]. To support application design, the static relationship between force, stroke, and voltage has been modelled [16–18], along with the dynamic behaviour induced by mechanical loads such as inertial effects and fluid viscous forces [19–21].

Regardless of the specific embodiment, a limitation of DFAs is that they do not naturally maintain a constant force when driven by a constant applied voltage. This happens because of leakage currents, which are different in the different dielectric layers, causing charges to accumulate at the interface [22,23]. Because of interface charge retention, the Maxwell stress generated between the electrodes decays over time, resulting in unzipping. A common solution adopted to prevent unzipping is the use of an inverting-polarity high-frequency driving voltage, which cyclically resets the charges accumulated at the interfaces [10,19].

Sîrbu et al. [22] provided a formal description of charge retention in terms of the electrical properties (namely, permittivity and resistivity) of the dielectric materials (polymer films and liquids), resorting to a description based on Maxwell–Wagner–Sillars polarization theory [24]. They observed and proved experimentally that force relaxation does not occur in the presence of so-called matched dielectric combinations, in which the polymeric film and the liquid have similar dielectric relaxation time constants [25]. Their work addressed charge retention by referring to the simple case of a parallel-plate capacitor in a blocked configuration, which is far from representing the complex kinematics of real zipping actuators and their stroke relaxation behaviour.

Cisneros et al. [26] developed a control-oriented modelling approach based on lumped RC circuit representations similar to those proposed in [22]. They described a multi-pouch Peano-HASEL actuator as a series of a constant and a variable capacitor, each in parallel to a resistor, to capture the effect of charge retention on unzipping. While their representation preserves the general physical structure given in [22] for a uniform parallel-plate capacitor, it makes use of model parameters that are not immediately interpretable in terms of the real actuator geometry and material properties, and largely relies on parameter identification. The modelling approach proposed by Cisneros et al. [26] was later adopted by some of the authors of the present paper to develop simulation-based control strategies for DFAs based on high-frequency voltage polarity inversion [27]. More recently, Xiong et al. [28] investigated stroke and force relaxation under constant voltage and adopted a formulation similar to that of Cisneros et al. to study control strategies based on alternating current (AC) driving, i.e., high-frequency voltage polarity inversion. Although their work provides valuable insights into the influence of AC driving on the dynamic response of electro-hydraulic actuators, the proposed formulation relies on lumped-parameter circuit models that require system identification, rather than being derived solely from the actuator geometry and material properties.

A framework capable of transferring the physical principles presented in [22] into complex DFA topologies is currently missing. Yet, accounting for charge retention-driven dynamics at the actuator level might help guide design decisions and design control strategies for DFAs [26].

This paper presents a physics-based modelling framework for DFAs, capable of describing the unzipping dynamics due to charge retention. The model builds upon a continuum formulation that describes the local distribution of charge and electric field within a device, bi-directionally coupled with a lumped parameter representation of the zipping mechanics. The electrical dynamics are captured using a simple RC formulation, which is nevertheless sufficient to describe charge-retention phenomena at the interface between dielectric layers. By modelling this effect, the proposed framework describes stroke relaxation both in DFAs in which the dielectric fluid sits at atmospheric pressure and closed pouch Peano-HASEL actuators, and it shows that the relaxation dynamics depend not only on the dielectric time constants of the materials, but also on device loading conditions and geometric parameters (e.g., the initial zipping angle).

With respect to previous works on dynamic modelling of charge retention in DFAs [22,26], the contribution of this article consists in (1) a fully-interpretable physics-based model that describes unzipping/relaxation of generic DFA actuators, given their geometry and material properties; (2) a unification and comparison of global DFA models (that describe the system response in terms of global actuator capacitance) and local models (that describe the system response in terms of local electrical variables and electrostatic force contributions); (3) an experimental quantitative analysis of the unzipping dynamics in two different DFA topologies (an open–pouch DFA and a Peano-HASEL), which validates the proposed formulation and provides insight into charge–relaxation effects at the actuator level. The general framework presented in this paper lays the foundation for local continuum modelling of DFAs, as it allows integrating local dependencies while maintaining a level of complexity much lower than that of bulk formulations involving volumetric discretizations of the dielectric domains. While the focus of this work is largely set on the slow dynamics induced by charge retention, the framework lends itself to extensions such as the incorporation of fluid-dynamic or visco-elastic loads, or more advanced electrical descriptions of the dielectrics' behaviour [29].

The rest of the paper is structured as follows. Section 2 presents a formulation for the DFA model, both in a continuum and discretized fashion. In Section 3 we investigate the influence of model parameters, electro-mechanical loads and geometrical design choice on the unzipping dynamics. In Section 4 we validate the framework against two different geometries. Finally, Section 5 presents the conclusions.

2. Electro-mechanical dynamics of DFAs

This section presents a general electro-mechanical formulation for the dynamics of DFAs, aimed at explaining how the actuator stroke evolves in time due to charge relaxation. A continuum electrical model for charges distribution [30] in a DFA is first introduced, and coupled with a lumped-parameter description of the device mechanical behaviour. The model is later recast in a discretized form and experimentally validated. The core idea is that the total electrostatic force generated by the device can be computed as a sum of contributions from infinitesimal parallel-plate multi-layer variable capacitors [31] into which the actuator can be ideally split. The electrostatic force depends on the charge distribution within the polymeric film and liquid layers of the capacitor, and it leads to actuator zipping, hence affecting its geometrical configuration.

We refer to a generic DFA architecture, and we assume that its deformation is describable by a single degree of freedom x, which is assumed to correspond to a linear contraction of the actuator. The following additional assumptions are made:

1. The electrical dynamics are governed by the leakage currents through the dielectric layers, which lead to so-called Maxwell–Wagner–Sillars polarization [24], here described using a simplified RC-based formulation. The model structure presented here can be in principle expanded to include advanced multi-branch circuit representations of the materials electrical behaviour [32].
2. Due to the materials resistivity, charges build up at the interfaces between dielectric layers [24,33,34]. For the aim of this study, space charges within the dielectric media are ignored.
3. Electrical properties of the materials, such as resistivity and permittivity, are assumed to be constant. Consequently, the material dielectric relaxation time is also constant.
4. In the zipped region, a residual liquid layer is present, whose thickness is constant during deformation and in different working conditions.
5. The thickness of the polymeric film layers is assumed constant upon zipping.
6. The length of the polymeric layers remains constant during deformation, i.e., the polymer layers are regarded as flexible but inextensible. This assumption describes a broad class of DFAs based on high-modulus dielectric films [2,6].

2.1. Continuum electrical model with lumped mechanical dynamics

The dynamic model of a DFA system is here formulated resorting to a set of continuum dynamic equations for the electrical variables, coupled with a mechanical equation of motion expressed in terms of a single kinematic degree of freedom $x = x(\tau)$, with τ representing the time. The electrode is ideally divided into infinitesimal material portions, whose position along the electrode is denoted by s, a curvilinear material coordinate defined along the electrode length; $s = 0$ corresponds to the length where the zipping starts. We denote $l_z = l_z(x)$ the length of the zipped portion of the electrode in a generic configuration.

Each infinitesimal portion is electrically represented by an RC network, consisting of a capacitor in parallel with a resistor to account for leakage currents. The dielectric layers are connected in series, leading to a circuital formulation analogous to that presented in [26]. The absolute permittivity ($\varepsilon = \varepsilon_0\varepsilon_r$, where ε_0 is the vacuum permittivity and ε_r is the relative permittivity of the dielectric) and resistivity (ρ) of the dielectric layers give rise to distinct electrical time constants ratios which, as shown in [22], lead to different charge retention dynamics across the dielectric layers.

Each infinitesimal material portion is assumed to be electrically independent of the others and subject to the same total applied voltage difference, as the distributed resistance of the electrodes is neglected [35]. Consequently, the global electrical model of the DFA consists of a continuous distribution of RC parallel branches. A visual interpretation of the continuum electrical formulation is represented in Fig. 1a. Note that, since the electrode is divided into material portions, the capacitances and resistances representing the constant-thickness film layer remain constant upon deformation, whereas the capacitances and resistances associated to the fluid gap portions are variable.

The electrical state of a single portion is described by the local surface charge densities $\sigma_l = \sigma_l(s,\tau)$ and $\sigma_f = \sigma_f(s,\tau)$ on the infinitesimal capacitors, modelling the liquid and the film layers respectively. We define $J_l = J_l(s,\tau)$ and $J_f = J_f(s,\tau)$ as the local leakage current densities flowing through the liquid and film dielectric layers, respectively. Modelling each dielectric layer as the parallel of a capacitor and a resistor (subject to the same voltage drop), Eq. (1) is obtained:

$$\begin{aligned} \frac{\sigma_l}{\varepsilon_l} &= \rho_l J_l \;\Rightarrow\; \sigma_l = \rho_l \varepsilon_l J_l = \tau_l J_l, \\ \frac{\sigma_f}{\varepsilon_f} &= \rho_f J_f \;\Rightarrow\; \sigma_f = \rho_f \varepsilon_f J_f = \tau_f J_f. \end{aligned} \tag{1}$$

Here, ρ_l denotes resistivity of the liquid, ε_l denotes the absolute permittivity of the liquid layer, i.e., $\varepsilon_l = \varepsilon_0\varepsilon_{r,l}$, where ε_0 is the vacuum permittivity and $\varepsilon_{r,l}$ is the relative permittivity of the liquid. The same definition applies to the polymeric film layer, i.e., ρ_f, $\varepsilon_f = \varepsilon_0\varepsilon_{r,f}$. The series connection of the dielectric layers implies, by current continuity, that

$$J_l + \dot{\sigma}_l = J_f + \dot{\sigma}_f. \tag{2}$$

Noting that the total driving voltage difference applied to the electrodes is $V = V(\tau)$, Kirchhoff's second law leads to

$$\rho_l\, t_l\, J_l + 2\,\rho_f\, t_f\, J_f = V. \tag{3}$$

where $t_l = t_l(s,x)$ denotes the local liquid thickness, and t_f denotes the thickness of a single polymer layer within the corresponding infinitesimal portion. As shown in Fig. 1a, t_l depends both on the material coordinate s and the instantaneous actuator stroke $x(\tau)$, which is kinematically related to the length l_z of the zipped portion. For $s \le l_z(x)$, i.e., within the zipped region, the liquid thickness is assumed to be constant and equal to a residual value $t_l = t_{l_z}$. Outside the zipped region, the liquid thickness depends on the actuator

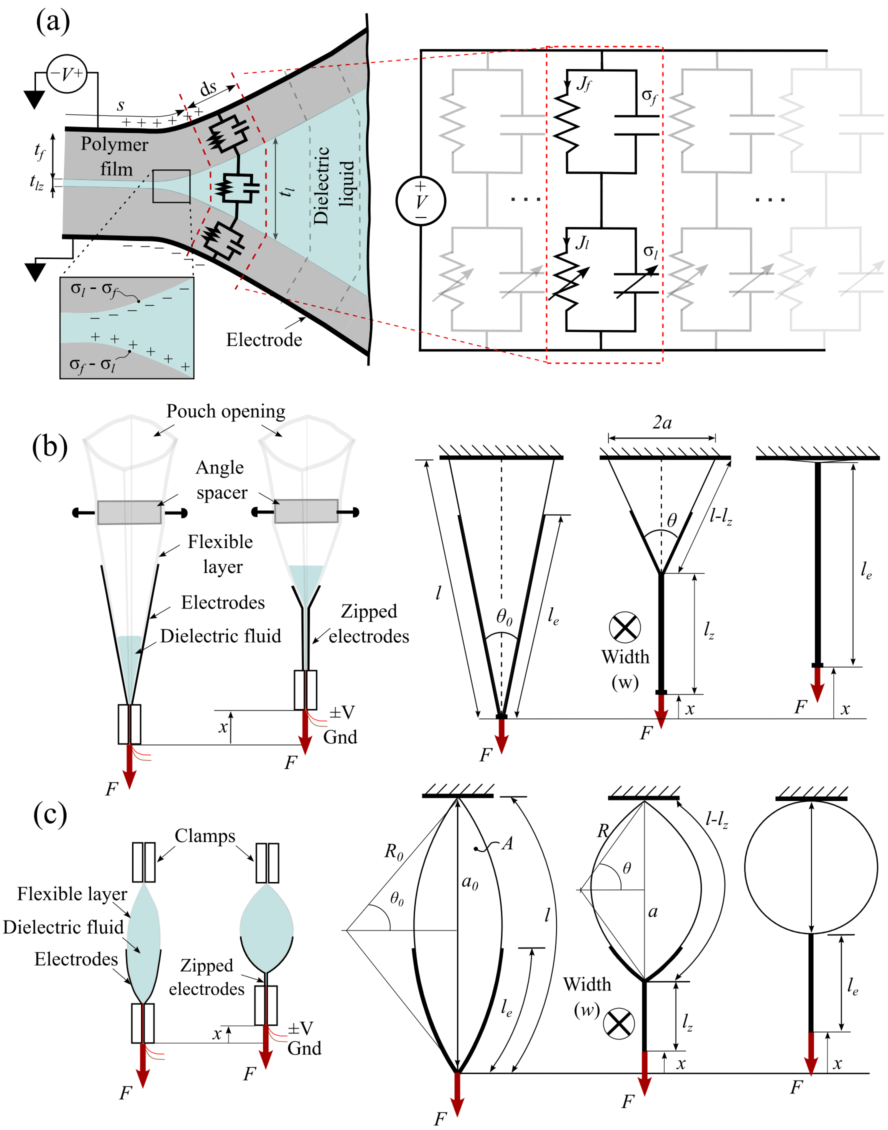

Fig. 1. (a) Continuum electrical formulation and circuit representation of a generic DFA. The electrode is divided into infinitesimal material portions, each constituted by an RC network made of constant and variable components. (b) Lateral cross section of the V-shaped actuator and its main kinematic parameters. (c) Lateral cross section of the Peano–HASEL actuator and its main kinematic parameters.

kinematics. For simplicity, here we define t_l as the fluid-filled distance between the polymeric layers measured perpendicularly to the zipping plane. While in reality a precise calculation of t_l should account for the shape and trajectory of the electric field lines within the fluid region, this assumption is considered sufficient to describe the DFA force dynamics, since the electric field rapidly decreases to zero outside of the zipped region.

Collecting the relations derived above, the electrical dynamics of the RC network shown in Fig. 1a, which electrically represents the overall DFA, can be described by the following system of differential–algebraic equations (DAEs):

$$\begin{cases} \sigma_l(s,\tau) = \tau_l J_l(s,\tau), \\ \sigma_f(s,\tau) = \tau_f J_f(s,\tau), \\ J_l(s,\tau) + \dot{\sigma}_l(s,\tau) = J_f(s,\tau) + \dot{\sigma}_f(s,\tau), \\ \rho_l\, t_l(s,x)\, J_l(s,\tau) + 2\,\rho_f\, t_f\, J_f(s,\tau) = V(\tau). \end{cases} \tag{4}$$

The electrostatic energy U_e stored in the dielectric layers is obtained from the volumetric electrostatic energy density. The volumes of the dielectrics within an infinitesimal portion are $d\Omega_l = t_l(s,x)\,w\,ds$ and $d\Omega_f = 2t_f\,w\,ds$, where w denotes the electrode width, leading to

$$U_e = \int_{\Omega_l} \frac{D_l^2}{2\,\epsilon_l}\,\mathrm{d}\Omega_f + \int_{\Omega_p} \frac{D_f^2}{2\,\epsilon_f}\,\mathrm{d}\Omega_f. \tag{5}$$

$D_l = D_l(s,\tau)$ and $D_f = D_f(s,\tau)$ denote the electric displacement fields across the liquid and polymer dielectric layers, respectively. As we assume that no volume charges are present within the materials and that charge only accumulates at the interfaces, the displacement is uniform across the layer and satisfies $D_l = \sigma_l$ and $D_f = \sigma_f$. Having l_e to denote the electrode length, we can express the electrostatic energy reported in Eq. (5) as

$$U_e = \frac{1}{2}\int_0^{l_e} \left(\frac{\sigma_l^2(s,\tau)\,t_l(s,x)}{\epsilon_l} + \frac{2\,\sigma_f^2(s,\tau)\,t_f}{\epsilon_f} \right) w\,\mathrm{d}s. \tag{6}$$

To cast the equation of motion of the actuator in terms of x, we call m the generalized mass associated to x, $U_m(x)$ is a generic elastic potential energy (e.g., due to external biasing springs or the bending stiffness of the flexible layers), and F is the externally applied force opposing x (i.e., acting against zipping). By treating the surface charge densities σ_l and σ_f as independent variables with respect to x, following the formalism commonly adopted in the Lagrangian analysis of electromechanical systems [36], and applying the Euler–Lagrange equation to the kinematic degree of freedom x, the following equation of motion is obtained:

$$m\,\ddot{x} + b\,\dot{x} + \frac{\partial U_m}{\partial x} + F + F_e(x,\tau) = 0, \tag{7}$$

where the electrostatic force F_e is given by

$$F_e(x,\tau) \equiv \frac{\partial U_e}{\partial x} = \frac{1}{2}\int_0^{l_e} \frac{\sigma_l^2(s,\tau)}{\epsilon_l}\,\frac{\partial t_l(s,x)}{\partial x}\,w\,\mathrm{d}s. \tag{8}$$

Notice that in Eq. (8) the explicit contribution from the polymeric film is disappearing and the total force comes from an integration of the charge density (and hence electric field) in the sole fluidic layer. This is consistent with the observation that, in a parallel-plate multi-layer capacitor in which only one layer has variable thickness, the force between the plates is proportional to the squared electric field in the variable layer [22]. This formulation generalizes lumped-parameter formulations for the electrostatic force that rely on the derivative of the DFA total capacitance with respect to x [16], which are only applicable in the presence of ideal dielectrics, with no charge accumulated at the interfaces.

Since the focus of this work is to analyse slow DFA stroke relaxations induced by the electrical dynamics and the temporal evolution of the electrostatic forces, simplified formulations are used for the mechanical terms. The model structure based on continuum electrical dynamics (4) and lumped mechanical Eq. (7), however, lends itself straightforwardly to the incorporation of additional force contributions that account for other effects, such as configuration-dependent inertia, or more sophisticated expressions for the viscous forces derived by fluid-dynamics [19]. The framework could be further extended to include more advanced dependences of the electrical properties on the state (e.g., the dependence of the materials resistivity on the electric field [37,38]). Moreover, the model could be extended to include the contribution of the dielectric films stretch (in topologies where this is present and functionally relevant) [3,39]. Doing so involves: (1) including contributions due to the materials' elastic energy in equation of motion (7); and (2) modifying the formulation for the continuum electrical dynamics to consistently account for variations in the material elements length (ds) and thicknesses.

2.2. Discretized model

The continuum model can be recast in a discretized form to enable numerical solution of the dynamic equations. Assuming that N material points ($N-1$ material portions) are uniformly distributed along the electrode length, Eq. (8) can be rewritten in a discretized form as follows:

$$F_{e_d} = \frac{w\,\Delta s}{2\,\epsilon_l}\sum_{j=1}^{N-1} \sigma_{l_j}^2\,\frac{\mathrm{d}t_{l_j}}{\mathrm{d}x}. \tag{9}$$

Δs denotes the material length associated with each discretized element and is defined as $\Delta s = l_e/(N-1)$. The j−th element corresponds to a material portion, and the corresponding thickness $t_{l_j} = t_{l_j}(x)$ is evaluated at the midpoint of the portion.

It is worth noticing that, in ideal static conditions (i.e., neglecting the dielectric layers resistivities), the electrostatic force can be derived upon differentiation of the equivalent layered capacitance C with respect to the mechanical degree of freedom x, as discussed in [16]. In that situation, the overall capacitance of the device can be well approximated by the sole capacitance C_z of the zipped region, where the total dielectric thickness is much smaller than that of the unzipped portion. Accordingly, the electrostatic force in static lossless conditions can be written as

$$F_{e,s} = -\frac{V^2}{2}\frac{\mathrm{d}C}{\mathrm{d}x} \simeq -\frac{V^2}{2}\frac{\mathrm{d}C_z}{\mathrm{d}x}, \qquad C_z = \frac{\epsilon_l\,\epsilon_f\,l_z\,w}{\epsilon_f\,t_{l_z} + 2\,\epsilon_l\,t_f}. \tag{10}$$

In the following, we demonstrate the convergence of F_{e_d} to $F_{e,s}$ in static conditions.

In static ideal conditions, the charge density σ_{l_j} on the liquid layer of the j−th discretized element can be calculated as in a capacitive voltage divider, and it reads as

$$\sigma_{l_j} = \frac{\epsilon_l\,\epsilon_f}{\epsilon_f\,t_{l_j} + 2\,\epsilon_l\,t_f}\,V. \tag{11}$$

By substituting Eq. (11) into Eq. (9), we obtain

$$F_{e_d} = \frac{w\,\Delta s}{2\,\varepsilon_l} \sum_{j=1}^{N-1} \frac{\varepsilon_l^2\,\varepsilon_f^2}{(\varepsilon_f\,t_{l_j} + 2\,\varepsilon_l\,t_f)^2} V^2 \frac{\mathrm{d}t_{l_j}}{\mathrm{d}x} = -\frac{w\,\varepsilon_l\,\varepsilon_f\,\Delta s\,V^2}{2} \frac{\mathrm{d}}{\mathrm{d}x}\left(\sum_{j=1}^{N-1} \frac{1}{\varepsilon_f\,t_{l_j} + 2\,\varepsilon_l\,t_f}\right). \tag{12}$$

where the second equality has been obtained by observing that t_f, ε_f and ε_l are constants, while t_{l_j} is a function of x.

Denoting by N_z the number of discretized elements within the zipped region, the summation in Eq. (12) can be approximated by retaining only the contributions from these elements, since the liquid thickness in the zipped region (t_{l_z}) is assumed to be uniform ($t_{l_j} = t_{l_z}$) and much smaller than that in the unzipped region (i.e., the terms into the summation are small/negligible in the unzipped region, where t_{l_j} is very high). Under these assumptions, Eq. (12) can be approximated as

$$F_{e_d} \simeq -\frac{w\,\varepsilon_l\,\varepsilon_f\,\Delta s\,V^2}{2} \frac{\mathrm{d}}{\mathrm{d}x}\left(\sum_{j=1}^{N_z} \frac{1}{\varepsilon_f\,t_{l_z} + 2\,\varepsilon_l\,t_f}\right). \tag{13}$$

Since the summand is constant (i.e., independent of j) within the zipped region and $l_z \simeq N_z\,\Delta s$, Eq. (13) simplifies to

$$F_{e_d} \simeq -\frac{w}{2} V^2 \frac{\varepsilon_l\,\varepsilon_f}{\varepsilon_f\,t_{l_z} + 2\,\varepsilon_l\,t_f} \frac{\mathrm{d}l_z}{\mathrm{d}x} = -\frac{V^2}{2}\frac{\mathrm{d}C_z}{\mathrm{d}x}, \tag{14}$$

which is identical to the expression of $F_{e,s}$ reported in Eq. (10). This proves that the proposed discretized model is consistent with a capacitance-based force calculation approach in static conditions.

Now, in order to easily implement the electrical dynamics of the system, we recast DAE (4) as a system of ordinary differential equations. The circuital representation of the device is slightly modified via a standard pseudo-transient continuation approach [40], by introducing, in each discretized portion, a fictitious resistor in series with the stack. With this modification, the electrical dynamics of each portion can be written in a state-space form by choosing the charge densities on the two capacitors as the state variables.

$$\begin{aligned}
\dot{\boldsymbol{\sigma}}_j &= \mathbf{A}_j\,\boldsymbol{\sigma}_j + \mathbf{B}_j\,V,\\
\boldsymbol{\sigma}_j &= \begin{bmatrix} \sigma_{l_j} \\ \sigma_{f_j} \end{bmatrix},\\
\mathbf{A}_j &= \begin{bmatrix} -\dfrac{(\rho t)_s + 2\rho_f t_f}{\varepsilon_f \rho_f (\rho t)_s} & -\dfrac{t_{l_j}(x)}{\varepsilon_f (\rho t)_s} \\ -\dfrac{2t_f}{\varepsilon_f (\rho t)_s} & -\dfrac{(\rho t)_s + \rho_f t_{l_j}(x)}{\varepsilon_f \rho_f (\rho t)_s} \end{bmatrix},\\
\mathbf{B}_j &= \frac{w\,\Delta s}{(\rho t)_s}\begin{bmatrix} 1 \\ 1 \end{bmatrix}.
\end{aligned} \tag{15}$$

The contribution of the series resistor enters the system matrices through the newly introduced term $(\rho t)_s$, which has the dimensions of $\Omega\,\mathrm{m}^2$ (namely, the product of a resistivity and a thickness). We remark that this quantity has no direct physical interpretation, and it is introduced for numerical reasons. This term affects the electrical charging time (and therefore the zipping dynamics) but does not influence the unzipping dynamics. Its value is therefore chosen to be sufficiently small to ensure that the charging time remains below the shortest time scale of interest, on the order of milliseconds.

2.3. Layouts: V-shaped and peano-HASEL actuators

In this work, the proposed framework is applied to two different actuator geometries. Figs. 1b–c illustrate the schematics of the devices and their corresponding kinematic parameters.

The V-shaped actuator (Fig. 1b) is inspired by the geometry proposed in [41]. The device consists of a pouch made of two initially flat dielectric membranes (each holding an electrode on its outer face), open at the top by a rigid spacer that confers the device cross sections a V-shaped and puts the dielectric liquid in communication with the atmospheric pressure. This geometry is adopted in this study to help isolate the electrical dynamics due to its simple kinematics, reduced edge effects, and operation of the fluid at atmospheric pressure. In addition, this layout provides uniform zipping and unzipping fronts during actuation, hence reducing potential sources of deviations from the kinematic assumptions used to build the models.

The kinematic parameters of the V-shaped DFA are introduced in Fig. 1b. The side length of the pouch (length of each polymer film, in the cross-section view of the figure) is denoted by l, while the semi-aperture of the actuator (i.e., the maximum spacing between the polymeric films, at the basis of the actuator) is denoted by a. The film is partly covered by an electrode with length l_e (with $l_e \leq l - a$), and width of w (perpendicular to the view of the figure). In a generically zipped configuration, the actuator stroke is denoted by x.

Under the assumption of inextensible polymer films (Section 2) and neglecting edge effects, the longitudinal length of the device (vertical length in Fig. 1b) in a partially zipped configuration is equal to the longitudinal length of the fully unzipped configuration (i.e., $x = 0$) minus the corresponding actuator stroke. This relationship can be expressed as

$$l_z + \sqrt{(l - l_z)^2 - a^2} = \sqrt{l^2 - a^2} - x. \tag{16}$$

Table 1
Baseline parameters for the V-shaped actuator used in simulations.

Parameter	Symbol	Value
Polymer thickness	t_f	25 µm
Residual liquid thickness (zipped)	t_{l_z}	10 µm
Relative permittivity (polymer)	$\varepsilon_{r,f}$	2.05
Relative permittivity (liquid)	$\varepsilon_{r,l}$	3.8
Resistivity (polymer)	ρ_f	1×10^{15} Ω m
Resistivity (liquid)	ρ_l	2×10^{12} Ω m
Polymer length	l	55 mm
Electrode width	w	60 mm
Electrode length	l_e	40 mm
Semi-aperture	a	11.9 mm
Reference voltage	V	6 kV
External load	F	5 N
Damping	b	10 Ns/m
Discretization points	N	1500

From (16), an expression for l_z can be derived explicitly as

$$l_z = \frac{2x\sqrt{l^2 - a^2} - x^2}{2(l + x - \sqrt{l^2 - a^2})}. \tag{17}$$

where l_z can take any value between 0 and l_e.

The zipping angle corresponding to each configuration is given by

$$\theta = 2 \arcsin\left(\frac{a}{l - l_z}\right), \tag{18}$$

We define the initial zipping angle θ_0 as the value of θ obtained for $l_z = 0$, corresponding to the unzipped configuration of the device.

The thickness $t_l(s, x)$ of the fluid layer (entering electrostatic Eq. (4) and the computation of the electrostatic force (8)) is calculated using the simplified assumption that the electric field lines are straight everywhere (parallel to those of the zipped region), resulting in

$$t_l(s, x) = \begin{cases} t_{l_z}, & \text{if } s \le l_z, \\ t_{l_z} + \dfrac{2(s - l_z)a}{l - l_z}, & \text{if } s > l_z. \end{cases} \tag{19}$$

The second layout considered in this study is the Peano-HASEL actuator [6], a well-known zipping device consisting of a liquid-filled, closed dielectric polymer pouch partially covered by compliant electrodes (Fig. 1c). Upon voltage application, the electrodes induce the liquid to form a bulge in the passive portion of the pouch. Although Peano-HASEL actuators are known to exhibit inhomogeneous zipping behaviour [19,42], which makes the analysis of the unzipping process particularly challenging, the geometry is employed in this work to further validate the proposed framework on a real-world device featuring a electro–hydraulic working principle, in which the electrostatic forces induce a pressurization of the dielectric fluid. The Peano-HASEL kinematics is modelled under the assumption that, in a generic zipped configuration, the device is composed by a zipped region (where the electrodes are flat), and a bulged region (enclosing the liquid), whose walls have the shape of symmetrical arcs of circumference. The equations for the Peano-HASEL geometry are taken from [17] and reported in Appendix A.

3. Parametric sensitivity analysis

In this section, simulations of the discretized model are used to investigate how device design and testing parameters influence the unzipping behaviour. The analysis focuses on the V-shaped actuator. A set of baseline parameter values is reported in Table 1, largely based on the experimental values used in Section 4. Unless otherwise specified, all simulations are conducted using those baseline parameters. The table lists the independent parameters, while the remaining ones can be derived from geometrical considerations. For the purposes of this study, inertial effects are neglected, as they are assumed to have a minor influence on the force balance for the considered masses and accelerations, which is expected to be dominated by viscous effects (e.g., due to fluid dynamics). Similarly, assuming a low bending stiffness for the polymer layers, the overall stiffness is neglected. The damping coefficient is selected such that, upon voltage application, the zipping time remains on the order of tens of milliseconds and, more generally, such that the mechanical dynamics are several orders of magnitude faster than the charge-accumulation dynamics.

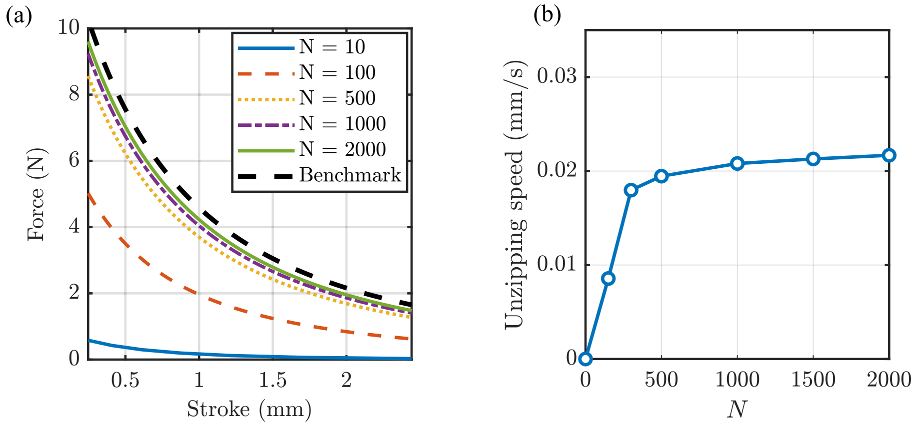

Fig. 2. Sensitivity and convergence analysis in statics and dynamics conditions with respect to the number of discretization elements N. (a) Static electrostatic force computed using Eq. (9), compared with the benchmark solution obtained from Eq. (10). (b) Average unzipping speed computed from the stroke time response to a voltage step input of 6 kV under an applied load of 5 N, having an initial zipping angle of $\theta_0 = 25°$.

3.1. Discretization

The number of elements N in which a device is discretized shall guarantee both a good static and dynamic description of the system. The expression in Eq. (10) can be used as a benchmark to determine the minimum number of discretization elements required to accurately describe the static force of the actuator. As shown in Fig. 2a, the force calculated from Eq. (9) approaches the benchmark static solution as the number of discretization elements, N, increases. As the solution converges towards the benchmark, the model becomes progressively less sensitive to further increases in the number of discretization elements.

The number of discretization elements N also influences the device dynamics. As shown in [22], the electrical time constant of the dielectric stack in the j−th portion is expressed as

$$\tau_j = \frac{2\,\tau_l\,\rho_f\,t_f + \tau_f\,\rho_l\,t_{l_j}(x)}{2\,\rho_f\,t_f + \rho_l\,t_{l_j}(x)}. \tag{20}$$

The coarser the discretization, the less accurate the representation of the thickness distribution along the electrode, particularly in the region adjacent to the zipping front, which experiences the largest variations in liquid thickness and therefore provides the dominant contribution to the electrostatic force (see Eq. (9)). Using a coarse discretization results in regions with overestimated values of t_{l_j} at the border of the zipped region (close to $s = l_z$), which imply larger local time constants and, therefore, slower simulated unzipping dynamics. Fig. 2b shows the simulated trend of the average unzipping speed, which, similarly to the static case, presents a converging trend as the number of discretization elements increases.

The simulations are performed by applying a voltage step input and monitoring the decay of the stroke x over a time window of 20 s. The unzipping speed is defined as the absolute value of the time average of the instantaneous velocity ($\dot{x} = dx/d\tau$) over the entire simulation. The required number of discretization elements can vary significantly depending on the device kinematics. For the set of parameters reported in Table 1 and the analyses presented in the following, $N = 1500$ is used for the V-shaped actuator. Based on Fig. 2b, this value of N is sufficient to guarantee convergence of the estimated unzipping speed. It is important to note that larger values of N come at the expense of higher computational cost.

3.2. Statics

The electrostatic force of the V-shaped DFA in static conditions is computed using Eq. (10) and reported in Fig. 3. Fig. 3a shows the actuator output force as a function of the stroke x at different applied voltages V, for the reference V-shaped actuator configuration of Table 1, characterized by an initial zipping angle $\theta_0 = 25°$. The actuator output force increases with the applied voltage and, similar to other DFA configurations [16], it decreases at higher strokes (i.e., as the zipping angle θ increases). Fig. 3b shows the force–stroke response (at a given reference voltage) of different embodiments of the V-shaped actuator, featuring different values of the initial zipping angle θ_0. The blocking force (i.e., the force at $x = 0$) increases as the initial zipping angle decreases. This happens because the liquid gap in the unzipped portion of the device is thinner for small values of θ_0, leading to larger electric fields. Finally, Fig. 3c shows the electrostatic force for different applied voltages as a function of the zipping angle θ (rather than the stroke x). This latter map holds true regardless of the initial zipping angle θ_0, and represents the response of different actuators embodiments, with fixed electrode width and dielectric film thickness, and different applied voltages. The independence of the static map in Fig. 3c on θ_0 highlights that the electrostatic force depends solely on the current zipping angle, i.e., on the geometry of the fluid gap at the boundary of the zipped region. Indeed, although the static stroke decreases as the initial zipping angle increases (due to the device kinematics), the equilibrium zipping angle (at given applied force and voltage) remains unchanged for different configurations featuring different values of θ_0.

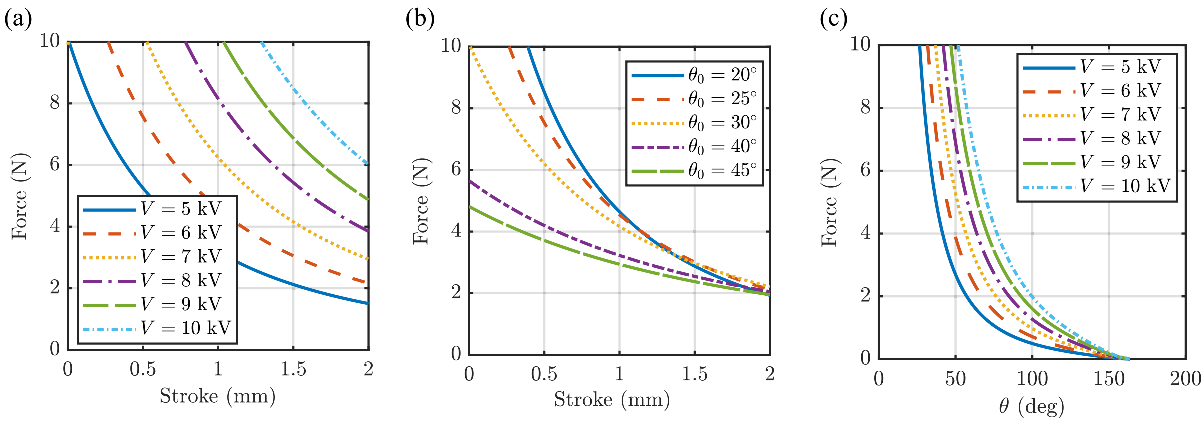

Fig. 3. Model predictions of the static force response of the V-shaped actuator. (a) Force–stroke response for applied voltages ranging from 5 to 10 kV, given an initial zipping angle $\theta_0 = 25°$. (b) Force–stroke response at 6 kV with initial zipping angles ranging from 20° to 45°. (c) Electrostatic force as a function of the instantaneous zipping angle for applied voltages ranging from 5 to 10 kV. For a given applied voltage, the force-zipping angle relationship is independent of the initial zipping angle; consequently, these curves hold valid for different actuator embodiments featuring different values of θ_0.

3.3. Driving voltage waveform

In Fig. 4a, we report the results of simulations in which different high-voltage (HV) input signals are applied to the DFA. The signals differ in polarity, frequency, and waveform. Simulations were performed using the formulation described in Section 2.2 and a discretization with $N = 1500$ elements, by applying a target voltage waveform on an initially still and uncharged actuator (see Table 1), and observing the resulting stroke trend. The application of a constant DC voltage leads to progressive unzipping (Fig. 4a - top left). Due to the strong electromechanical coupling, the system exhibits nonlinear dynamics, and the resulting stroke relaxation does not follow a purely exponential trend. This differs from the force relaxation of blocked parallel-plate configurations, where the electrostatic force is independent of the system kinematics and the response follows first-order linear dynamics with an exponential decay (see [22]). Here, the actuator stroke relaxation is slower than exponential, with a predicted unzipping speed that is nearly-constant in time.

Applying a square wave voltage signal in which the polarity is quickly reversed from positive to negative and vice-versa allows the device to maintain a stable steady-state stroke, with fluctuations that decrease in magnitude if the frequency of inversion is increased (Fig. 4a - second column), consistently with experimental observations reported in previous works [17,22,43]. When a same polarity is maintained over successive actuation cycles (Fig. 4a - bottom left), charge builds up at the interfaces, resulting in a progressive reduction of the stroke. Overall, these trends match the expected device behaviours reported in previous experimental works [3,22].

In Fig. 4b, we simulate the effect of different mechanical static loads applied to the device. Higher loads lead to smaller strokes which, because of the device kinematics, result in smaller zipping angles. Smaller zipping angles facilitate the retention of a zipped configuration, translating into slower unzipping dynamics.

3.4. Material properties

Fig. 4c shows how the DFA stroke response to a voltage step changes in the presence of different material combinations. We consider a case with given dielectric liquid properties, and different polymeric films with decreasing resistivities, moving towards a matched materials combination, in which the dielectric time constant of the polymer ($\tau_f = \rho_f \varepsilon_f$) approaches that of the liquid ($\tau_l = \rho_l \varepsilon_l$). As proven in [22], there is no surface charge accumulation in the case of matched dielectrics, with $\tau_f/\tau_l \simeq 1$, and therefore the device retains a constant stroke. For a ratio $\tau_f/\tau_l > 10$, the dynamics is governed by the time constant of the liquid, and it is roughly independent of τ_f.

3.5. Geometrical design

In Fig. 4d, for a fixed applied force and voltage step (see Table 1), we analyse the response of different actuators featuring different values of the initial zipping angle, θ_0, in order to investigate the effect of the geometry on the unzipping dynamics. The simulations qualitatively show that smaller initial angles lead to slower unzipping dynamics. This trend holds true in a range of values of θ_0, but it reverts at high values of the initial angle. To corroborate this, in Fig. 4e we report the value of the average unzipping speed calculated over different simulations, each with a different value of θ_0. The average unzipping speed is calculated by observing the actuator stroke over a time window of 20 s, following the application of a voltage step. At large initial angles (here, over 30°) the average unzipping speed decreases, as a consequence of a reduction in the actuator static stroke (cf. Fig. 3).

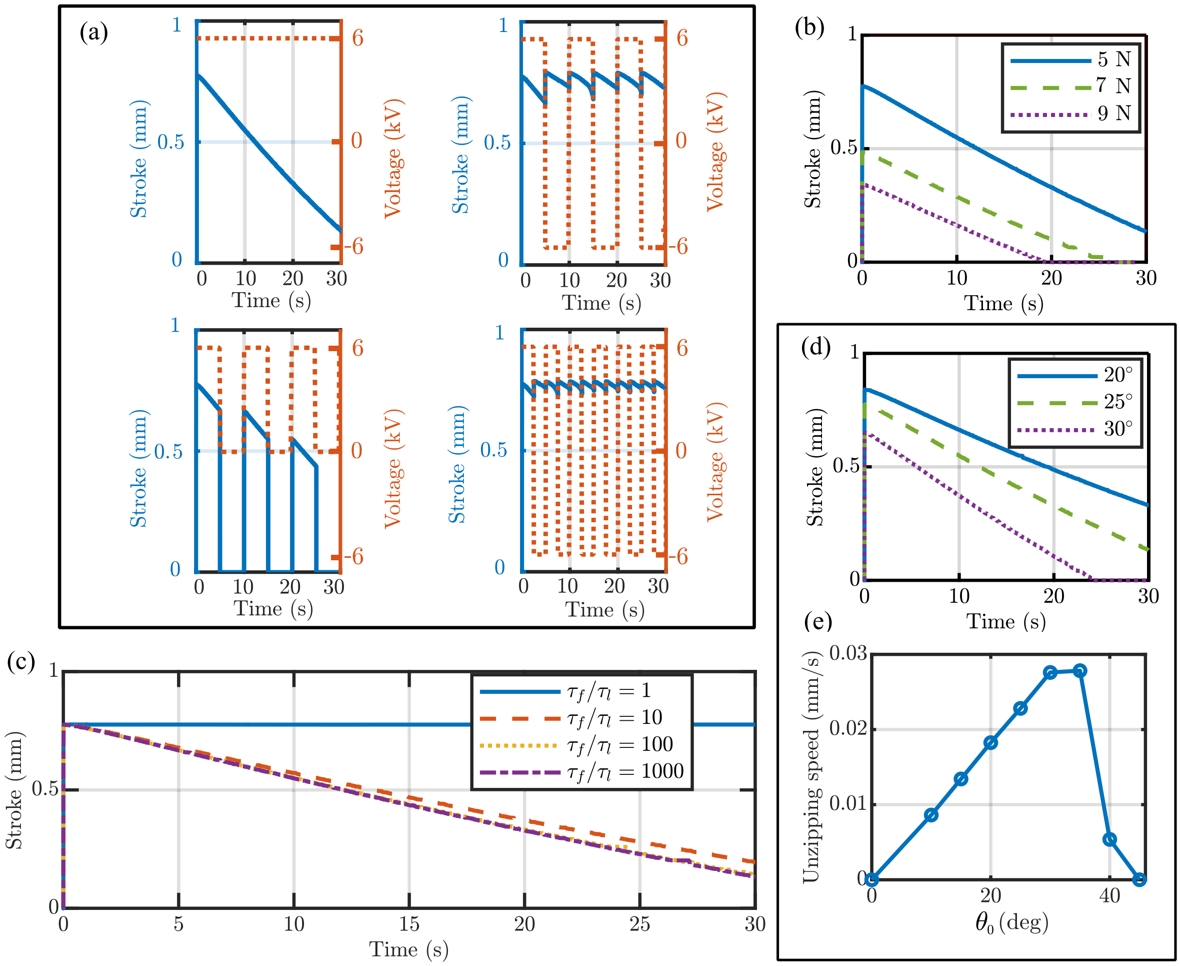

Fig. 4. Simulation sensitivity analyses of the unzipping response of a V-shaped DFA. (a) Comparison of the dynamic stroke response under voltage supply signals with different frequencies, polarities, and waveforms. Stroke response to a voltage step for: (b) different mechanical loads; (c) different liquid–polymer combinations with different electrical properties. In this case, the liquid resistivity is kept constant at $\rho_l = 2{\times}10^{12}\ \Omega\,\mathrm{m}$, while the polymer film resistivity is varied, resulting in different ratios of the dielectric time constants of the two materials; (d) different initial zipping angles, θ_0; (e) average unzipping speed as a function of the initial zipping angle under a DC voltage.

4. Experimental validation

To validate the proposed framework, this section presents experimental results obtained on both a V-shaped actuator and a Peano-HASEL actuator. A large portion of the experimental validation was conducted on the V-shaped actuator which, due to its simple kinematics, provides an ideal platform for model validation, allowing the unzipping phenomenon to be investigated with a stronger focus on the electrical dynamics and material properties. The Peano-HASEL geometry is then used to further validate the model on a representative real-world actuator. Results on the Peano-HASEL geometry are reported with the purpose of demonstrating that the proposed theory also holds for electro-hydraulic (i.e., HASEL-like) actuators, where the electrostatic forces induce fluid pressurization. These latter results should, however, be interpreted with caution, as they may be affected by the abovementioned zipping inhomogeneities [42].

4.1. Setups and device fabrication

The experiments were carried out on a custom test-bench, as represented in Fig. 5a. A real-time target machine (Speedgoat Performance Target, 3.1 GHz, combined with an IO131 16-bit module) was used for data acquisition and control. The target machine sends low-voltage control signals to a high-voltage amplifier (Trek 10/10B-HS), which is used as the power supply. The high-voltage amplifier features a built-in voltage monitor, which is used to measure the output voltage through the DFA. The stroke of the devices

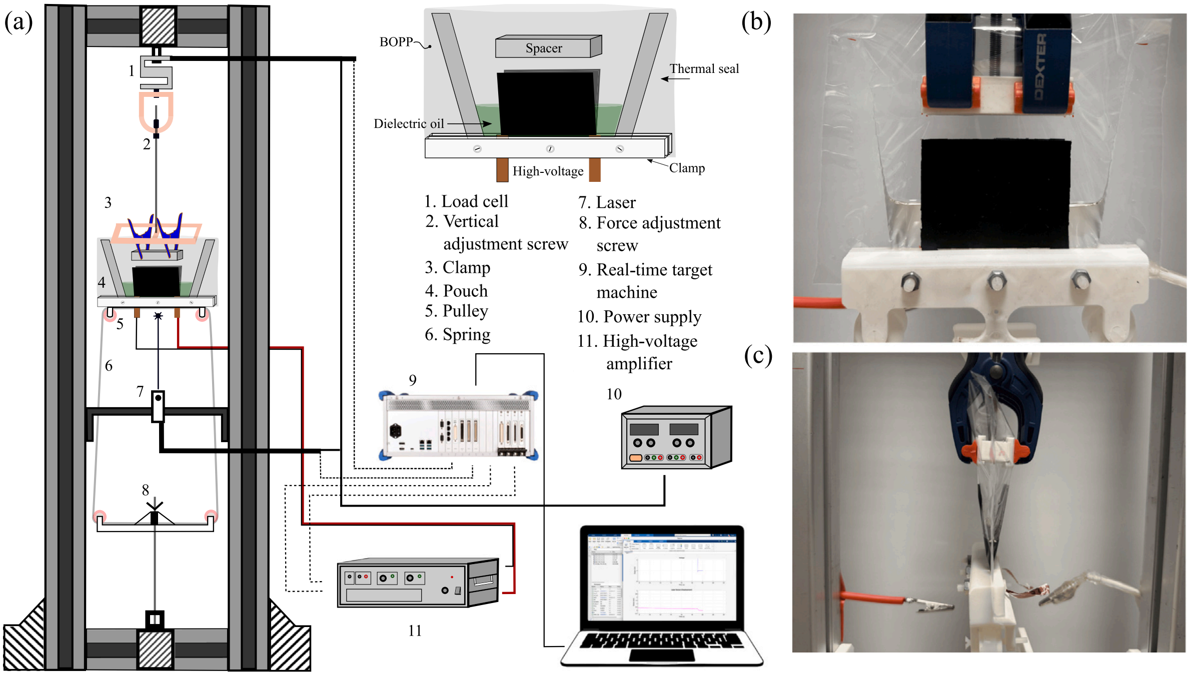

Fig. 5. (a) Experimental setup schematic with the V-shaped actuator installed. All setup components are listed in the image, and their specifications are given in Section 4.1. (b) Front view of the V-shaped actuator (photograph). (c) Side view of the V-shaped actuator (photograph).

is measured using a precision laser displacement sensor (optoNCDT 1320–25), while the applied force is measured using a load cell (ME KD24s-20N).

The applied force is generated by elongating a custom-made silicone spring (made of Dragon Skin 20NV) with a length and stiffness such that the millimetric contractions produced by the actuators result in a negligible variation of the applied force, as presented in previous works [9,22]; therefore, the force can be considered constant during actuation. The force applied in the different tests is regulated by moving the fixed end of the silicone band. In the case of the Peano-HASEL actuator, a static weight is attached to the device. For the latter, we observed that applying the force at a single, central point results in a more homogeneous zipping behaviour.

Both the V-shaped actuator and the Peano-HASEL actuator were fabricated using Multi-Plastics' thermally sealable biaxially oriented polypropylene (BOPP) HSF5114H (25 μ m) as the polymeric layer, Cargill FR3 as the dielectric fluid, and Ted Pella DAG-T-502 carbon paint for the electrodes. The dielectric fluid is not pre-treated, either thermally or electrically, but is simply taken directly from the bottle. The heat-sealable layers of the BOPP films are soldered by depositing a 3D-printed PLA stencil at 220 °C using a Bambu Lab X1-Carbon printer, as proposed in [15]. To ensure uniform heat distribution and prevent excessive melting of the BOPP layers, the molten PLA is deposited onto a protective polyimide single-sided adhesive layer placed on top of the BOPP films, with the adhesive part facing up, to promote adhesion of the printed PLA layer.

While the Peano-HASEL actuator is fully filled with liquid, only a limited amount of liquid (3 ml) is used in the V-shaped actuator, as shown in Fig. 5b. This partial filling does not affect the electro-mechanical behaviour of the device sensibly, since during zipping most of the electrostatic force is generated by the portion of the electrodes located near the zipping front, whereas the regions where the electrodes are farther apart contribute only marginally [2,18]. Moreover, in the unzipped portion of the device, far from the zipping front, the large electrode separation results in an electric field well below the breakdown threshold, even in the presence of air in the portion of the gap far from the zipping region, as recently observed in [44]. During actuation, the liquid is pushed upward towards the region where the polymer layers approach each other, thereby ensuring smooth and stable zipping behaviour. To facilitate the liquid evacuation process, the thermally bonded perimeter features a trapezoidal shape that creates lateral space for the liquid (on the electrode side) and limits the rise in liquid level during zipping. Furthermore, during consecutive tests, the inner part of the device remains wet from previous cycles. The very first test performed on a device is not used for data processing, in order to ensure that the layers are covered by at least a thin liquid film.

The devices are equipped with 3D-printed supports that allow for the application of the desired load and also allow the laser to measure the contraction. For the V-shaped actuator, the initial opening angle θ_0 is set by means of exchangeable rigid spacers located at the top of the pouch and held in place by elastic clips (Fig. 5c). A 100 kΩ resistor is put in series with the device in order to limit current flow in the system in the case of failures.

4.2. Experimental results

Tests are performed according to a fixed routine. Since this work focuses on electrically-driven unzipping dynamics, all the presented tests use constant DC voltage signals preceded by a charge reset stage with a duration of 3 s, in which a high-frequency (30 Hz) square-wave polarity inversion with 100% duty cycle at the same voltage used during the test is applied, as shown in Fig. 6a. This charge reset stage is used to bring the device to a neutral charge state with respect to the previous test. After charge reset, a DC voltage is held, and unzipping is monitored. To ensure repeatable unzipping behaviour under given test parameters, each test was repeated five times.

Fig. 6b reports the effect of changing the applied force on the unzipping dynamics. The experimental trends show that the stroke relaxation follows a smooth dynamics, with a stroke decrease that clearly exhibits a slower-than-exponential trend. Some tests exhibit a quick stroke relaxation immediately after the charge reset cycle. This behaviour may be attributed to fast electrical dynamics, possibly due to the presence of volume charges that rapidly flow through the liquid gap at each polarity inversion, causing large current peaks over short time intervals [45], or mechanical dynamics (e.g., overzipping effect [19]) due to electro-mechanical interaction. Because the liquid resistivity is modelled in a simplified manner, assuming a constant and spatially uniform ohmic resistivity, these phenomena cannot be captured within the theoretical framework presented in this work. Yet, as shown in the following sections, the simplifications used in this work quantitatively and qualitatively capture the relevant trends and the orders of magnitude of the mean relaxation speed in different conditions.

4.3. Validation

For the purpose of validation, both static and dynamic validations are considered. Simulations related to the V-shaped actuator are performed using the parameter values reported in Table 1. The parameters used for Peano-HASEL simulations are reported in Appendix A. For the dynamic simulations, $N = 1500$ elements were used for the V-shaped DFA, and $N = 500$ elements were used for the Peano-HASEL actuator, following a convergence analysis like that described in Section 3.1. It should be noted that the number of discretization elements required for convergence strongly depends on the actuator kinematics. Consequently, the number of elements needed to achieve convergence may vary significantly across different actuator topologies, as observed in the present case.

All the parameters used in the model (geometrical quantities, the materials permittivity, the residual thickness of liquid in the zipped region) come from direct measurements, as explained in Appendix B. Only the resistivities ρ_l and ρ_f have been fitted to the experiments. As observed in previous works [22], the combination of BOPP with standard dielectric liquids (here, FR3) represents a combination with $\tau_f \gg \tau_l$. From the results in Section 3.4 (see Fig. 4c), we know that, in this situation, the unzipping dynamics weakly depends on τ_f (provided that it is large enough), and it is dominated by τ_l instead. We therefore use a resistivity $\rho_f = 1\times10^{15}\ \Omega\,\mathrm{m}$ for BOPP, similar to the order of magnitude measured in [22]. For the liquid, providing an estimate of the resistivity is more complicated because

- The resistivity might depend on the state (e.g., the local electric field to which the liquid is subject). [46]
- Available resistivity measurements are obtained using cells in which the liquid is in direct contact with metal electrodes—a situation that is not representative of the DFA working conditions [47].

For these reasons, the liquid resistivity ρ_l, a constant best-fit value was identified a posteriori, by comparing experiments and model predictions. Given the high uncertainty on the dielectric liquid resistivity, and its possible dependence on the system state, we also identified ranges (around the reference selected value of ρ_l) whose corresponding simulations provide upper and lower bounds that encompass most of the experimental observations. Considering a range of liquid resistivity values enables a sensitivity analysis of the model response with respect to this parameter. We believe that this approach demonstrates that the proposed framework correctly predicts the order of magnitude of the observed phenomena and, more importantly, captures the trends of the unzipping dynamics with respect to the governing design and working parameters.

4.3.1. Static validation

A validation of the static V-shaped actuator model is first performed. Similar to previous validation studies on DFA static models [17], we compare the static stroke achieved upon voltage application, for different applied forces and voltages. Experimentally, the static stroke is defined as the mean value of x measured during the charge-reset stage described in Section 4.2. The polarity inversion frequency is faster than the charge-accumulation dynamics, therefore the device stroke remains approximately constant around its equilibrium position. The theoretical static stroke is computed according to Eq. (10). The results of the static validation are reported in Fig. 7. The model effectively captures the static behaviour of the device. The stroke (especially at higher voltages) is slightly overestimated by the model, possibly because of edge effects introduced by the thermally bonded joints, which introduce an unmodelled mechanical constraint. The mean force deviation from the model is 6.4%.

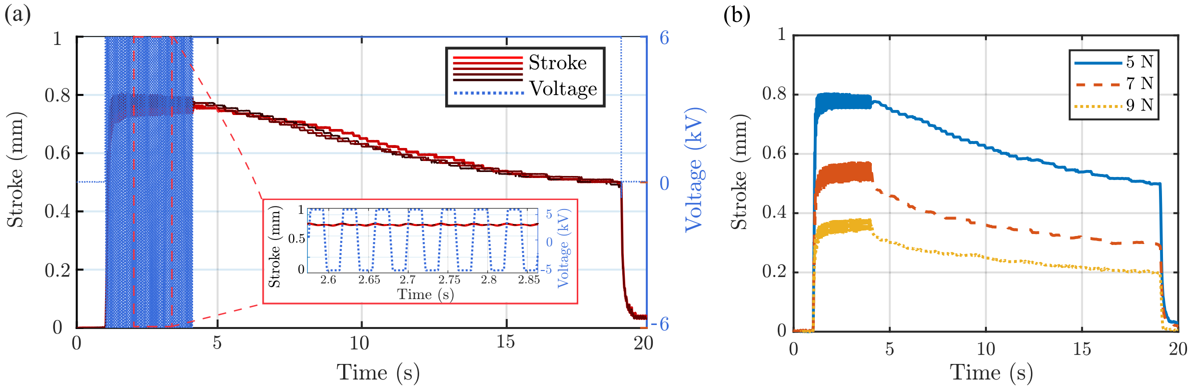

Fig. 6. (a) Experimental stroke response over five tests of a V-shaped actuator subjected to a constant DC voltage and a static load (6 kV and 5 N), preceded by a high-frequency (30 Hz) square-wave polarity inversion. (b) Step response at different applied forces with 6 kV as input and $\theta_0 = 25°$.

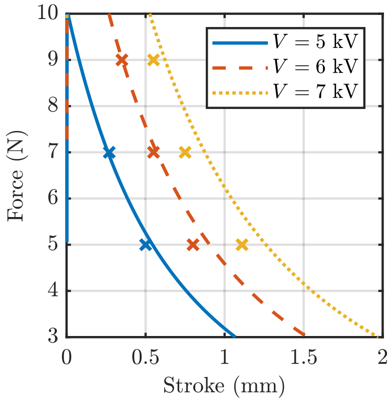

Fig. 7. Static validation via experimental measurement of the V-shaped actuator static response for different electro-mechanical load combinations. Single point data represent the experimental results, while curves represent model predictions (Eq. (10)).

4.3.2. Dynamic validation

The metric used to characterize the unzipping dynamics is the average unzipping speed, introduced in Section 3.1 and defined here as the absolute value of the time average of the instantaneous stroke velocity over the test, after the charge reset phase. The accuracy of the model is evaluated by assessing whether, using a fixed set of parameters, the model is able to predict the average unzipping speed and its dependence on geometrical and functional parameters. Specifically, we experimentally investigate the predicted dependence of the unzipping speed on the applied load, the initial zipping angle, and the applied voltage.

With reference to the V-shaped actuator, Figs. 8a–c compare the numerical predictions with the experimental results to assess the capability of the model to capture the unzipping speed under different parametric variations. Each plot reports the overall trend of the unzipping speed as a function of a design or loading parameter. Black markers refer to experimental data, whereas dashed lines refer to simulations with different values of ρ_l. A single reference value, $\rho_l = 2.5\times10^{12}$ Ωm, was identified as providing the best overall agreement across all the experiments. The corresponding prediction is shown as the dashed red curve. To define a representative range of liquid resistivity values within which the experimental results can be described, and to illustrate the sensitivity of the model to this parameter, two additional simulations are reported (light red curves), corresponding to $\rho_l = 2.0\times10^{12}$ and 3.0×10^{12} Ωm. The experimental results are presented as black error bars obtained from five repetitions of each test, following the procedure illustrated in Fig. 6a. Specifically, the central marker represents the mean unzipping speed computed from the five experimental repetitions, while the upper and lower ends of the error bars correspond to the maximum and minimum values measured across the experiments.

For each of the selected values of the liquid resistivity ρ_l, the model successfully captures the experimentally observed trends, namely that the unzipping speed increases with increasing initial zipping angle (Fig. 8a), decreases with increasing applied force (Fig. 8b), and increases with increasing applied voltage (Fig. 8c). It is worth remarking that these trends hold within the specific working ranges considered for the tests, as predicted by the model, and they might revert over different intervals. For instance, in the case of the zipping angle, one should expect a monotonic increase in unzipping speed only in a finite range, as the unzipping speed would equal 0 both at $\theta_0 = 0$ and at large values of θ_0, as in both cases the stroke would tend to 0. The ability of the model to capture unzipping speed trends associated with the design parameters of the DFA (here, θ_0) is a result of explicitly considering

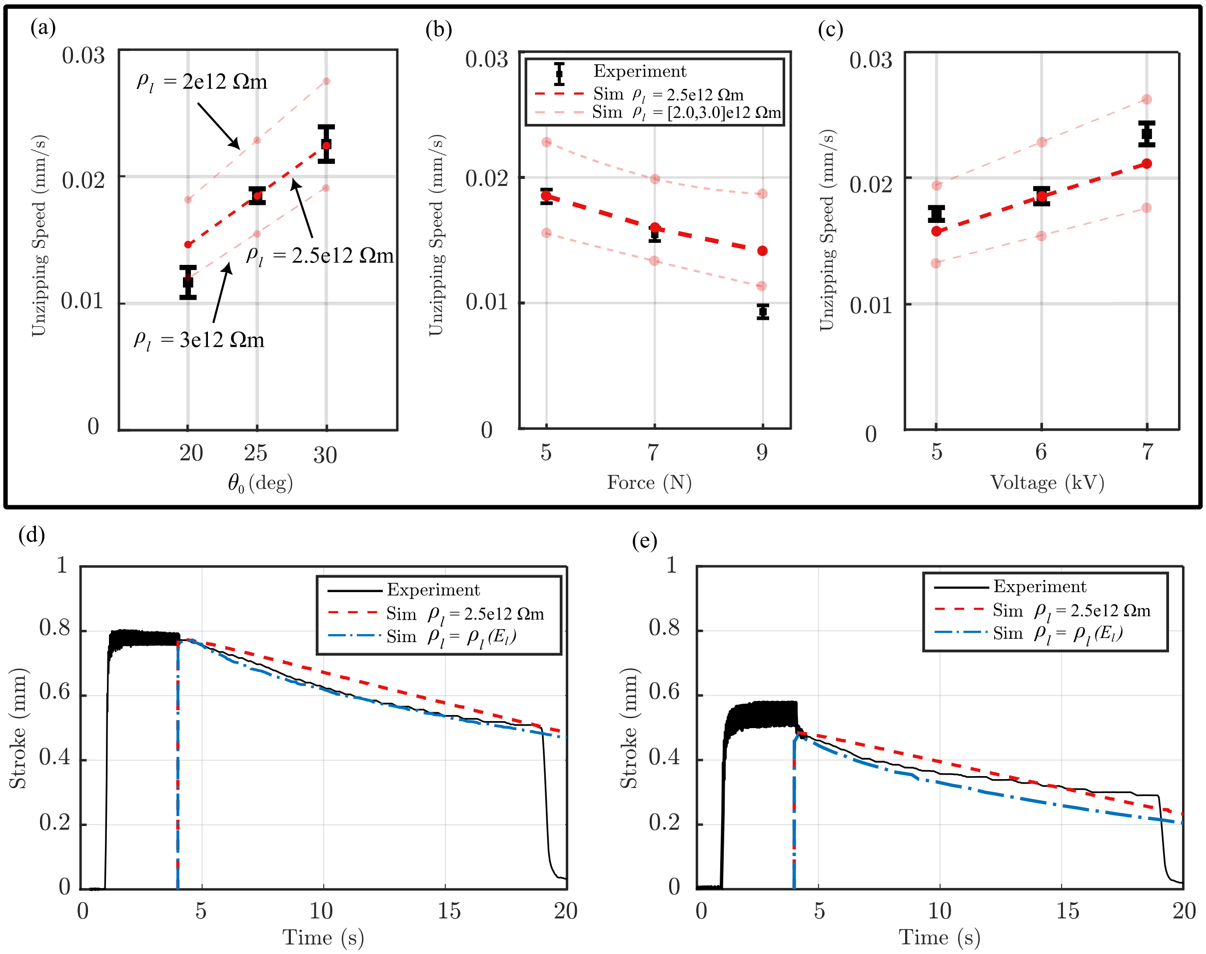

Fig. 8. V-shaped actuator dynamic validation under different testing conditions (applied force and DC voltage) and geometrical implementations (initial angle θ_0). The resistivity values ρ_f and ρ_l are kept constant across all tests. (a) 5 N–6 kV, at different initial angles. (b) 25°–6 kV, at different applied forces. (c) 5 N–25°, at different voltages. (d) 5 N–6 kV–25°, comparison of experimental and simulated time responses. (e) 7 N–6 kV–25°, comparison of experimental and simulated time responses. The red dashed line refers to simulations with constant ρ_l, whereas the blue dash-dot curve refers to simulation with field-dependent ρ_l.

the device kinematics and a geometrical derivation of the electrostatic force (Eq. (9)) within the model. This prediction capability suggests that the proposed framework can be used to guide design of DFAs, in applications where the unzipping dynamics are relevant.

Figs. 8d–e show two representative time responses from which the previous plots are generated. In these panels, a single experimental result (black curve) is compared with two simulation results. The red curve represents the simulated stroke relaxation obtained using the reference constant value of the liquid resistivity, $\rho_l = 2.5\times10^{12}$ Ωm. The model captures the overall time evolution of the real system but while the simulation predicts a nearly constant unzipping speed, the experimentally observed unzipping speed gradually decreases over time. This behaviour may result from higher-order or nonlinear electrical conduction mechanisms acting on shorter time scales than those associated with the stroke relaxation [47]. For this reason, assuming a constant liquid resistivity represents a strong simplification.

To corroborate our hypothesis that the discrepancies between the experimental stroke trends and the model predictions (red dashed lines in Fig. 8d–e) might come from the assumption of a constant ρ_l, we performed simulations with a field dependent liquid resistivity, $\rho_l = \rho_l(E_l)$, where $E_l = D_l/\varepsilon_l$ is the local electric field in the liquid. Such a field-dependent resistivity can be incorporated in the model (namely, in Eq. (4)) without changing the model structure or the governing equations. The model-predicted trends of the actuator stroke relaxation for a field–dependent ρ_l are represented by the blue dash-dot curves in Fig. 8d–e. For the sake of simplicity, we considered a linear dependence of ρ_l on the electric field:

$$\rho_l = m_\rho\, E_l + q_\rho, \tag{21}$$

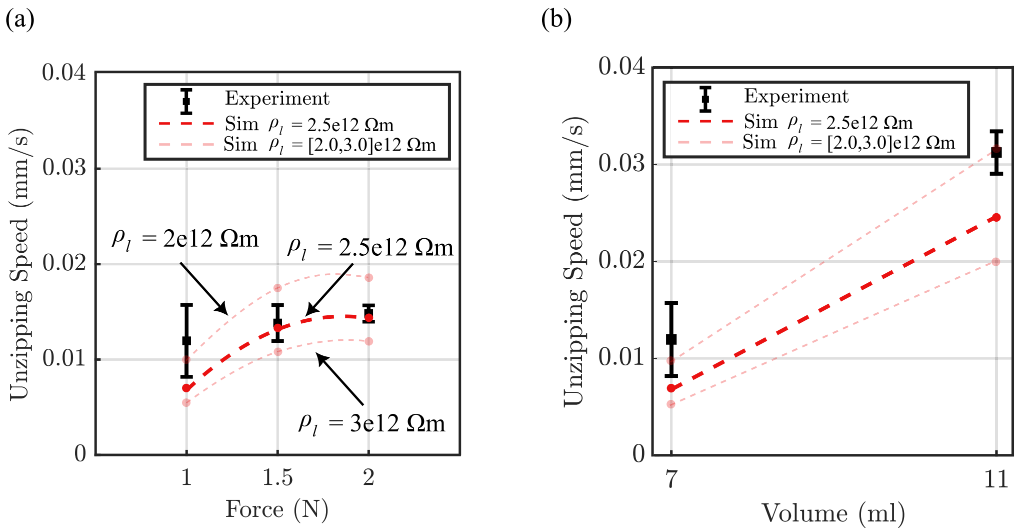

Fig. 9. Peano–HASEL actuator dynamic validation under different testing and geometrical conditions. The resistivity values ρ_f and ρ_l are the same as those used for the V-shaped actuator. (a) 7 ml–7 kV, at different applied forces. (b) 1 N–7 kV, at different liquid volumes in the pouch. Different liquid volumes correspond to different initial zipping angles, similarly to the V-shaped actuator.

where the parameters $m_\rho = -3.34 \times 10^5$ m^2/A and $q_\rho = 20 \times 10^{12}\,\Omega\,\mathrm{m}$ were identified by fitting the experimental relaxation curve reported in Fig. 8d. Since the resistivity is now evaluated independently for each discretized material portion, it varies both spatially and temporally during the unzipping process. The results in Fig. 8d–e show that, assuming that ρ_l decreases with E_l, leads to stroke trends that are qualitatively closer to the experimental ones, with an unzipping speed that decreases in time. This happens because, as the DFA unzips, the electric field in the remanent zipped portion progressively decreases, causing an increasing in ρ_l and a consequent deceleration of the unzipping process.

While the resistivity expression in Eq. (21) provides a close description of the dynamic response of the test in Fig. 8d (which was used to calibrate the parameters of Eq. (21)), the same expression does not reproduce the response reported in Fig. 8e with equal accuracy. This suggests that, while a field–dependent resistivity can explain the progressive reduction in unzipping speed observed in the experiments, identifying an exact and generalizable expression for $\rho_l(E_l)$ is a non-trivial task, which demands for dedicated studies.

To characterize the range of resistivity values reached during the variable-resistivity simulation in Fig. 8d and compare it with the constant base-case value considered before, we continuously monitored (in simulation) the resistivity of the material portion located at the boundary between the zipped and unzipped regions. This portion is expected to have the greatest influence on the unzipping dynamics, as it experiences the largest variations in liquid thickness and therefore dominates the evolution of the electrostatic force. The resulting mean resistivity is $\rho_l = 2.91 \times 10^{12}\,\Omega\,\mathrm{m}$, with a standard deviation of $0.98 \times 10^{12}\,\Omega\,\mathrm{m}$. This value is close to and consistent with the previously-assumed constant value of $2.5 \times 10^{12}\,\Omega\,\mathrm{m}$.

In Fig. 9, we present an analysis of the unzipping speed in a Peano-HASEL actuator. To mitigate uncertainties due to inhomogeneous unzipping, which are common in this actuator topology [19], we selected testing conditions under which a flat zipping front can be obtained. Specifically, the device was tested at large strokes (low forces and high voltages), with short electrode lengths (less than 50% of the pouch length), and it was suspended through a single hanging point to guarantee vertical alignment. Tests were done considering different forces and different device implementations with different liquid volume (resulting in pouches with different initial aspect ratio). In this case, the same simulation band that was used to describe the V-shaped actuator – $\rho_l \in [2 \times 10^{12}, 3 \times 10^{12}]\,\Omega\mathrm{m}$ – does not fully encompass the experimental results, although the observed trends are captured and the predicted unzipping speeds are of the same order of magnitude as the experimental measurements. The unzipping behaviour of this real-world actuator is inherently more complex to predict due to higher-order effects that influence both the homogeneity of the zipping front [19] and the unzipping dynamics [19]. Also in this case, however, the framework fully captures the orders of magnitude of the unzipping speed, and their dependence on the functional parameters. Importantly, these latter results prove that unzipping in Peano–HASEL actuators (in which the fluid pressure plays a functional role) can be explained within the boundaries of the proposed framework, i.e., the unzipping speed can be quantified without explicitly referring to the dielectric fluid pressure, which, in the present formulation, remains an unquantified internal state variable.

4.3.3. Discussion

It is worth noting that the range of liquid resistivity values considered for the validation – $\rho_l \in [2 \times 10^{12}, 3 \times 10^{12}]\,\Omega\mathrm{m}$ – is lower, although of the same order of magnitude, than the values reported in the literature for FR3 dielectric oil [48], despite the application of stronger electric fields, which are known to reduce the effective resistivity of insulating liquids [45] (as postulated in Eq. (21) and in the variable-field simulation results of Fig. 8d–e). This observation is nevertheless consistent with the fact that conventional resistivity measurements are typically performed with the liquid in direct contact with metallic electrodes.

Under these conditions, the measured resistivity results from two concurrent contributions: bulk conduction due to intrinsic charge carriers within the liquid, and charge injection from the metallic electrodes [49,50]. The latter mechanism alters the measured current and may lead to an overestimation of the apparent liquid resistivity, thereby masking the intrinsic bulk conduction properties of the dielectric liquid [33,51]. In contrast, in the present experiments, charge injection from the electrodes is effectively prevented by the highly insulating polymer films separating the electrodes from the liquid.

5. Conclusion

In this paper, we presented a physics-based general framework to model and describe the unzipping dynamics of dielectric fluid actuators (DFAs) induced by charge retention at the polymer-liquid interfaces. The model couples a continuum formulation describing the charge and electric-field distribution across the device with a lumped-parameter description of the mechanical dynamics, which is described by a single degree of freedom, based on an assumption of the device kinematics. In its current form, the framework is primarily employed to describe dynamics induced by charge retention; however, it can be extended to incorporate more complex mechanical phenomena (fluid–dynamic effects) and electrical phenomena (bulk charge effects and field-dependent resistivity). While the presented formulation applies to DFAs with flexible but inextensible dielectric polymer layers, the framework can be extended to stretchable DFAs by accounting for the dependence of the polymer thickness on the stroke, and by adopting higher-order elastic models.

We validated the theoretical framework by performing tests in which we measured the unzipping speed, under DC voltages, of different DFAs: an actuator in which the dielectric fluid remains at atmospheric pressure during actuation, and a hydraulically amplified self-healing electrostatic (Peano-HASEL) actuator. The results show that the proposed model captures the fundamental trends and parametric dependencies of the unzipping dynamics, with uncertainties mainly associated with the electrical resistivity of the liquid, considered as a constant and uniform parameter in the formulation. In particular, the initial zipping angle, the applied static load, and the voltage input signal are found to significantly affect the unzipping behaviour, with trends that can be predicted by our model.

The proposed framework can therefore be used to inform device design and manufacturing optimization, as well as to develop efficient control strategies aimed at mitigating or compensating undesirable unzipping behaviours.

Building upon the formulations presented here, future works will focus on model order reduction approaches, aimed at reducing the model to decrease the number of electrical branches used in the discretization, to provide computationally-efficient control-oriented formulations. Effort will also be put in formulating models able to describe complex conduction mechanisms and electrochemistry in dielectric fluids, to provide reliable estimates of the fluids resistivity in the working conditions of DFAs.

CRediT authorship contribution statement

Marco Riva: Writing – original draft, Visualization, Investigation, Formal analysis, Data curation. **Rajat Chaudhary:** Writing – review & editing, Visualization, Investigation, Data curation. **Sandra Dirè:** Writing – review & editing, Supervision, Methodology. **Luca Fambri:** Writing – review & editing, Supervision, Methodology. **Marco Fontana:** Writing – review & editing, Methodology, Conceptualization. **Giacomo Moretti:** Writing – original draft, Project administration, Methodology, Funding acquisition, Formal analysis, Conceptualization.

Declaration of competing interest

The authors declare that they have no known competing financial interests or personal relationships that could have appeared to influence the work reported in this paper.

Acknowledgements

The authors would like to acknowledge Multi-Plastics Inc. and Cargill Türkiye, who kindly provided the BOPP films and FR3 liquid used for the tests.

The authors would like to thank Massimo De Cinque Quintili Catalucci for the technical support provided during the experimental activities.

Parameter	Symbol	Value
Polymer thickness	t_f	25 μm
Residual liquid thickness (zipped)	t_{l_z}	10 μm
Relative permittivity (polymer)	$\varepsilon_{r,f}$	2.05
Relative permittivity (liquid)	$\varepsilon_{r,l}$	3.8
Resistivity (polymer)	ρ_f	$1 \times 10^{15}\ \Omega\,\mathrm{m}$
Resistivity (liquid)	ρ_l	$2 \times 10^{12}\ \Omega\,\mathrm{m}$
Polymer length	l	35 mm
Electrode width	w	88 mm
Electrode length	l_e	17 mm
Liquid volume	Ω_f	7 ml
Reference voltage	V	7 kV
External load	F	1 N
Damping coefficient	b	10 N s/m
Discretization points	N	500

(a)

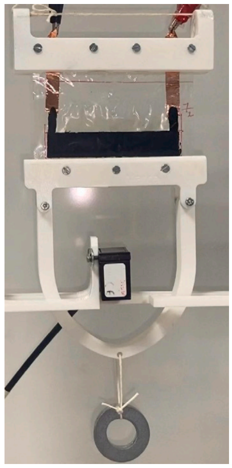

(b)

Fig. 10. (a) Baseline parameters of the Peano–HASEL actuator used in the sensitivity analysis. (b) Photograph of the experimental setup used to characterize the Peano–HASEL actuator geometry. The actuator shown contains 7 ml of FR3 dielectric oil.

Appendix A. Peano-HASEL kinematics

The following appendix describes the kinematics of the Peano-HASEL layout, as shown in Fig. 1c. The relations below are used to define the initial geometrical configuration of the Peano–HASEL actuator. The polymer length l and the volume of liquid Ω_f contained in the pouch are selected as independent parameters, together with the electrode width, w. Based on these quantities, the initial configuration of the device is fully defined by solving the following set of equations:

$$\begin{aligned} A &= \frac{\Omega_f}{w}, \\ A &= 2(\theta_0 R_0^2 - R_0^2 \sin\theta_0 \cos\theta_0), \\ l &= 2R_0\theta_0, \\ a_0 &= 2R_0 \sin\theta_0. \end{aligned} \tag{22}$$

Here, A denotes the cross-sectional area of the pouch, θ_0 is half of the initial curvature angle of the pouch, and R_0 is the corresponding radius of curvature, as shown in Fig. 1c. The quantity a_0 represents the initial longitudinal length of the pouch.

Once the initial configuration is defined, the actuator kinematics are obtained by allowing the curvature angle θ to vary between its initial value θ_0 and $\pi/2$. At each configuration, the geometry is determined by enforcing volume preservation and by assuming the polymer layers to be flexible but inextensible.

The actuator stroke x is then computed for each configuration by solving the coupled system

$$\begin{aligned} & l - l_z - 2R\theta = 0, \\ & A - 2\theta R^2 + (a_0 - l_z)R\cos\theta = 0, \\ & x = a_0 - l_z - 2R\sin\theta. \end{aligned} \tag{23}$$

The thickness of the fluid layer is consequently given by:

$$t_l(s,x) = \begin{cases} t_{l_z}, & \text{if } s \le l_z, \\ t_{l_z} + 2\,R\left(\cos\left(\theta - \frac{(s-l_z)}{R}\right) - \cos\theta\right), & \text{if } s > l_z, \end{cases} \tag{24}$$

The list of values used to compute the simulations related to the Peano-HASEL actuator are reported in Tab. shown in Fig. 10a. The corresponding actuator used for experimental validation is shown in Fig. 10b

Appendix B. Parameters identification

In this appendix, we report how the parameters used in the model simulations are identified experimentally. The nominal value of the polymeric film thickness t_f, given by the manufacturer, is cross-checked using an optical microscope. The relative permittivity ε_r of both materials is obtained by measuring the capacitance of capacitors with known geometry using an LCR meter (RS-LCX-100). For the polymer films, rectangular electrodes are created on two opposite faces of a film. In the case of the liquid, two laminated

PCB are engraved using a CNC machine and positioned at a known distance. The capacitor is then submerged in the dielectric liquid, which fills the gap between the electrodes.

The residual liquid thickness t_{l_z} in the zipped region is estimated by measuring the capacitance of the full DFA in the zipped condition by applying a step signal having a superimposed high-frequency sinusoidal signal, using voltage and force levels sufficient to reach a fully zipped configuration, and measuring the associated current [52,53]. The voltage is measured via the voltage monitor of the power supply while the current is measured using a current sensor built in house (same as in [3]). The liquid thickness t_{l_z} is obtained from the total measured capacitance, knowing the permittivity and thickness of the films, and the permittivity of the oil.

Appendix C. List of symbols

General formulation

Symbol	Unit	Description
b	Ns/m	Damping coefficient
s	m	Curvilinear material coordinate
t_f	m	Polymer film thickness
t_l	m	Local liquid thickness
t_{l_z}	m	Residual liquid thickness (zipped region)
l_z	m	Length of the zipped electrode portion
m	kg	Mass
m_ρ	m^2/A	Fitting parameter for $\rho_l(E)$ (see Eq. (21))
q_ρ	Ωm	Fitting parameter for $\rho_l(E)$ (see Eq. (21))
x	m	Actuator stroke
C	F	Capacitance
C_z	F	Capacitance of the zipped portion
D_f	C/m^2	Electrical displacement in the polymer film
D_l	C/m^2	Electrical displacement in the liquid
E_l	V/m	Electric field in the liquid
F	N	Applied force
F_e	N	Electrostatic force
$F_{e,s}$	N	Electrostatic force (static capacitance model)
J_f	A/m^2	Leakage current density in the polymer film
J_l	A/m^2	Leakage current density in the liquid
U_e	J	Electrostatic potential energy
U_m	J	Elastic potential energy
V	V	Applied voltage
ε_0	F/m	Vacuum permittivity
ε_f	F/m	Dielectric film permittivity (absolute)
ε_l	F/m	Dielectric liquid permittivity (absolute)
$\varepsilon_{r,f}$	–	Dielectric film permittivity (relative)
$\varepsilon_{r,l}$	–	Dielectric liquid permittivity (relative)
ρ_f	Ωm	Polymer film resistivity
ρ_l	Ωm	Liquid resistivity
σ_f	C/m^2	Surface charge density on the polymer film layers
σ_l	C/m^2	Surface charge density on the liquid layer
τ	s	Time (variable)
τ_f	s	Dielectric time constant of the polymer film
τ_l	s	Dielectric time constant of the liquid
Ω_f	m^3	Dielectric polymer volume
Ω_l	m^3	Dielectric liquid volume

Discretized formulation

Symbol	Unit	Description
$\mathbf{A}_j$, $\mathbf{B}_j$	vars.	State-space matrices
F_{e_d}	N	Electrostatic force (approxim.)
N	–	Number of material points
$(\rho t)_s$	Ωm^2	Series resistance contribution (fictitious)
σ_{f_j}	C/m^2	Charge density on the $j-$th portion of the polymer film
σ_{l_j}	C/m^2	Charge density on the $j-$th portion of the liquid
$\boldsymbol{\sigma}_j$	C/m^2	Charge density vector for the $j-$th element

τ_j	s	Time constant of the j–th portion (stack)
Δs	m	Material element portion length

V-shaped actuator

Symbol	Unit	Description
a	m	Semi–aperture (see Fig. 1b)
l	m	Side length (see Fig. 1b)
l_e	m	Electrode length (see Fig. 1b)
w	m	Electrode width (see Fig. 1b)
θ	rad	Zipping angle (generic configuration)
θ_0	rad	Zipping angle (initial)

Peano-HASEL actuator

Symbol	Unit	Description
a_0	m	Pouch initial longitudinal length (see Fig. 1c)
l	m	Pouch side length (see Fig. 1c)
l_e	m	Electrode length (see Fig. 1c)
w	m	Electrode width (see Fig. 1c)
A	m^2	Cross-section area
R	m	Pouch curvature radius (generic configuration) (see Fig. 1c)
R_0	m	Pouch curvature radius (initial) (see Fig. 1c)
θ	rad	Half of the curvature angle (generic configuration) (see Fig. 1c)
θ_0	rad	Half of the curvature angle (initial) (see Fig. 1c)
Ω_f	m^3	Liquid volume

Appendix D. Supplementary data

Supplementary material related to this article can be found online at https://doi.org/10.1016/j.ymssp.2026.114929.

Data availability

Data will be made available on request.

References

[1] P. Rothemund, N. Kellaris, S.K. Mitchell, E. Acome, C. Keplinger, HASEL artificial muscles for a new generation of lifelike robots—recent progress and future opportunities, Adv. Mater. 33 (2021) 2003375.
[2] M. Taghavi, T. Helps, J. Rossiter, Electro-ribbon actuators and electro-origami robots, Sci. Robot. 3 (2018) eaau9795.
[3] I.-D. Sîrbu, G. Moretti, G. Bortolotti, M. Bolignari, S. Dirè, L. Fambri, R. Vertechy, M. Fontana, Electrostatic bellow muscle actuators and energy harvesters that stack up, Sci. Robot. 6 (2021) eaaz5796.
[4] E. Acome, S.K. Mitchell, T. Morrissey, M. Emmett, C. Benjamin, M. King, M. Radakovitz, C. Keplinger, Hydraulically amplified self-healing electrostatic actuators with muscle-like performance, Science 359 (2018) 61–65.
[5] S.K. Mitchell, X. Wang, E. Acome, T. Martin, K. Ly, N. Kellaris, V.G. Venkata, C. Keplinger, An easy-to-implement toolkit to create versatile and high-performance HASEL actuators for untethered soft robots, Adv. Sci. 6 (2019) 1900178.
[6] N. Kellaris, V. Gopaluni Venkata, G.M. Smith, S.K. Mitchell, C. Keplinger, Peano-HASEL actuators: Muscle-mimetic, electrohydraulic transducers that linearly contract on activation, Sci. Robot. 3 (2018) eaar3276.
[7] E. Leroy, H. Shea, Hydraulically amplified electrostatic taxels (haxels) for full body haptics, Adv. Mater. Technol. 8 (2023) 2300242.
[8] S. Hoh, T. Helps, R.S. Diteesawat, M. Taghavi, J. Rossiter, Electro-lattice actuator: a compliant high-contractile active lattice structure, Smart Mater. Struct. 30 (2021) 125034.
[9] I.-D. Sîrbu, A. Mazzotta, U. Tosi, D. Bortoluzzi, V. Mattoli, G. Moretti, M. Fontana, Vacuum-gap electrostatic multilayer actuators for space robotics, Nat. Commun. (2025).
[10] G. Grasso, S. Rosset, H. Shea, Fully 3d-printed, stretchable, and conformable haptic interfaces, Adv. Funct. Mater. 33 (2023) 2213821.
[11] F. Hartmann, L. Penkner, D. Danninger, N. Arnold, M. Kaltenbrunner, Soft tunable lenses based on zipping electroactive polymer actuators, Adv. Sci. 8 (2021) 2003104.
[12] R.S. Diteesawat, T. Helps, M. Taghavi, J. Rossiter, Electro-pneumatic pumps for soft robotics, Sci. Robot. 6 (2021) eabc3721.
[13] H. Sun, L. Zhang, C. Tao, Y. Huang, J. Liu, J. Wang, Stretchable dielectric fluid pumps for soft fluid power systems, Adv. Mater. Technol. 10 (2025) e00798.
[14] F. Hartmann, M. Baskaran, G. Raynaud, M. Benbedda, K. Mulleners, H. Shea, Highly agile flat swimming robot, Sci. Robot. 10 (2025) eadr0721.
[15] S.-D. Gravert, E. Varini, A. Kazemipour, M.Y. Michelis, T. Buchner, R. Hinchet, R.K. Katzschmann, Low-voltage electrohydraulic actuators for untethered robotics, Sci. Adv. 10 (2024) eadi9319.
[16] G. Moretti, M. Duranti, M. Righi, R. Vertechy, M. Fontana, Analysis of dielectric fluid transducers, in: Electroactive Polymer Actuators and Devices (EAPAD) XX, vol. 10594, SPIE, 2018, pp. 142–154.
[17] N. Kellaris, V.G. Venkata, P. Rothemund, C. Keplinger, An analytical model for the design of Peano-HASEL actuators with drastically improved performance, Extrem. Mech. Lett. 29 (2019) 100449.
[18] Y. Xu, E. Burdet, M. Taghavi, Electromechanical model for electro-ribbon actuators, Int. J. Mech. Sci. 275 (2024) 109340.

[19] P. Rothemund, S. Kirkman, C. Keplinger, Dynamics of electrohydraulic soft actuators, Proc. Natl. Acad. Sci. 117 (2020) 16207–16213.
[20] Y. Yeh, N.E.C. Pinto, Y. Wu, K. Rabenorosoa, Y. Le Gorrec, Modeling and position control of the HASEL actuator via port-hamiltonian approach, IEEE Robot. Autom. Lett. 7 (2022) 7100–7107.
[21] T. Hainsworth, I. Schmidt, V. Sundaram, G.L. Whiting, C. Keplinger, R. MacCurdy, Simulating electrohydraulic soft actuator assemblies via reduced order modeling, in: 2022 IEEE 5th International Conference on Soft Robotics (RoboSoft), IEEE, 2022, pp. 21–28.
[22] I.-D. Sîrbu, D. Preninger, D. Danninger, L. Penkner, R. Schwödiauer, G. Moretti, N. Arnold, M. Fontana, M. Kaltenbrunner, Electrostatic actuators with constant force at low power loss using matched dielectrics, Nat. Electron. 6 (2023) 888–899.
[23] E. Rumley, P. Rothemund, S. Zhang, N. Kellaris, C. Keplinger, Characterization of charge retention effects in HASEL actuators, in: Electroactive Polymer Actuators and Devices (EAPAD) XXIV, SPIE, 2022, p. PC120420B.
[24] T. Prodromakis, C. Papavassiliou, Engineering the Maxwell–Wagner polarization effect, Appl. Surf. Sci. 255 (2009) 6989–6994.
[25] W.T. Coffey, Dielectric relaxation: an overview, J. Mol. Liq. 114 (2004) 5–25.
[26] N. Cisneros, Y. Wu, K. Rabenorosoa, Y. Le Gorrec, Dynamic modeling of a curling HASEL actuator using the port hamiltonian framework with experimental validation, Mechatronics 109 (2025) 103342.
[27] M. Riva, S. Dirè, L. Fambri, G. Rizzello, G. Moretti, Model-based position control of dielectric fluid actuators via high-frequency modulation, in: Electroactive Polymer Actuators, Sensors, and Devices (EAPAD) 2026, vol. 13945, SPIE, 2026, pp. 18–31.
[28] Q. Xiong, G. Tan, X. Zhou, D. Li, R.C.-H. Yeow, AC square wave voltage-driven series elastic electrohydraulic actuator with stable and smooth displacement output for robotic applications, IEEE/ASME Trans. Mechatronics (2024).
[29] T.L. Sounart, T.A. Michalske, K.R. Zavadil, Frequency-dependent electrostatic actuation in microfluidic mems, J. Microelectromech. Syst. 14 (2005) 125–133.
[30] J.R. Melcher, Continuum electromechanics, vol. 2, MIT press Cambridge, MA, 1981.
[31] Y. Zimmels, Thermodynamics of electroquasistatic systems: The parallel plate capacitor, J. Electrost. 38 (1996) 283–301.
[32] P. Semančík, R. Cimbala, I. Kolcunová, Dielectric analysis of natural oils, Acta Electrotech. et Inform. No 7 (2007) 3.
[33] M. Cullingford, A. Zaky, M.Z. Eldine, R. Hawley, Influence of electrode coatings on conduction currents in transformer oil, Nature 199 (1963) 1082–1083.
[34] T. Nakamura, A. Yamamoto, Modeling and control of electroadhesion force in dc voltage, Robomech J. 4 (2017) 18.
[35] D. Vignotto, A. Cherubini, I.-D. Sîrbu, M. Fontana, G. Moretti, An investigation of the electrical dynamics in electroactive polymer transducers with resistive electrodes, Smart Mater. Struct. 33 (2024) 095022.
[36] W. Manhães, R. Sampaio, R. Lima, P. Hagedorn, J.-F. Deü, Lagrangians for electromechanical systems, Mecánica Comput. 36 (2018) 1911–1934.
[37] Y. Sha, Y. Zhou, D. Nie, Z. Wu, J. Deng, A study on electric conduction of transformer oil, IEEE Trans. Dielectr. Electr. Insul. 21 (2014) 1061–1069.
[38] Y. Chen, L. Agostini, G. Moretti, M. Fontana, R. Vertechy, Dielectric elastomer materials for large-strain actuation and energy harvesting: a comparison between styrenic rubber, natural rubber and acrylic elastomer, Smart Mater. Struct. 28 (2019) 114001.
[39] S. Kirkman, P. Rothemund, E. Acome, C. Keplinger, Electromechanics of planar HASEL actuators, Extrem. Mech. Lett. 48 (2021) 101408.
[40] T.S. Coffey, C.T. Kelley, D.E. Keyes, Pseudotransient continuation and differential-algebraic equations, SIAM J. Sci. Comput. 25 (2003) 553–569.
[41] F. Gao, P. Zhang, Y. Zhang, M. Xu, Electrostatically driven multi-chamber accordion origami air pump, IEEE Robot. Autom. Lett. (2025).
[42] P. Rothemund, N. Kellaris, C. Keplinger, How inhomogeneous zipping increases the force output of Peano-HASEL actuators, Extrem. Mech. Lett. 31 (2019) 100542.
[43] E.H. Rumley, D. Preninger, A. Shagan Shomron, P. Rothemund, F. Hartmann, M. Baumgartner, N. Kellaris, A. Stojanovic, Z. Yoder, B. Karrer, et al., Biodegradable electrohydraulic actuators for sustainable soft robots, Sci. Adv. 9 (2023) eadf5551.
[44] H.-J. Joo, T. Fukushima, X. Li, A. Shagan Shomron, S.J.A. Koh, P. Rothemund, C. Keplinger, Ultralight soft electrostatic actuators based on solid-liquid-gas architectures, Nat. Commun. 17 (2026) 1929.
[45] L. Yang, S.M. Gubanski, Y.V. Serdyuk, J. Schiessling, Dielectric properties of transformer oils for hvdc applications, IEEE Trans. Dielectr. Electr. Insul. 19 (2013) 1926–1933.
[46] N. Lavesson, L. Walfridsson, O. Hjortstam, J. Schiessling, Modelling and measurement of field dependent resistivity of transformer oil, in: 2014 IEEE 18th International Conference on Dielectric Liquids, ICDL, IEEE, 2014, pp. 1–4.
[47] T. Gabler, K. Backhaus, S. Großmann, R. Fritsche, Dielectric modeling of oil-paper insulation systems at high dc voltage stress using a charge-carrier-based approach, IEEE Trans. Dielectr. Electr. Insul. 26 (2019) 1549–1557.
[48] P. Rumpelt, F. Jenau, Investigation on dc conductivity of alternative insulating oils as an application for hvdc converter transformers, in: 2017 IEEE 19th International Conference on Dielectric Liquids, ICDL, IEEE, 2017, pp. 1–6.
[49] E. Forster, The metal/liquid interface: the charge injection process, IEEE Trans. Electr. Insul. (2007) 524–528.
[50] M. Russel, P. Selvaganapathy, C. Ching, Effect of electrode surface topology on charge injection characteristics in dielectric liquids: An experimental study, J. Electrost. 72 (2014) 487–492.
[51] M. Zein Eldine, A. Zaky, R. Hawley, M. Cullingford, Influence of electrode coatings on space charge distributions in transformer oil, Nature 201 (1964) 1309–1311.
[52] T.A. Gisby, B.M. O'Brien, I.A. Anderson, Self sensing feedback for dielectric elastomer actuators, Appl. Phys. Lett. 102 (2013).
[53] G. Rizzello, D. Naso, A. York, S. Seelecke, A self-sensing approach for dielectric elastomer actuators based on online estimation algorithms, IEEE/ASME Trans. Mechatronics 22 (2016) 728–738.